Nanoscale

PAPER

View Article Online
View Journal | View Issue

Cite this: *Nanoscale*, 2025, **17**, 2252

Rational design of $NiCo_2O_4$@carbon hollow spheres as a high-performance electrode material for flexible supercapacitors†

Naveen T. Bharanitharan,[a] Durgalakshmi Dhinasekaran,[b] M. R. Ashwin Kishore,[c] Balakumar Subramanian[d] and Ajay Rakkesh Rajendran *[a]

Received 11th November 2024,
Accepted 3rd December 2024

DOI: 10.1039/d4nr04709e

rsc.li/nanoscale

The design of innovative, flexible electrode materials with high electrochemical performance is critical for the development of next-generation supercapacitors. Here, we report the rational synthesis of $NiCo_2O_4$@carbon hollow spheres, engineered *via* a metal–organic framework (MOF)-templated strategy, as a high-performance electrode material for flexible supercapacitors. The unique hollow structure of $NiCo_2O_4$@carbon enhances ion accessibility and electron transport, while the carbon layer provides structural stability and conductivity, significantly boosting energy storage capabilities. Structural characterization confirms the well-defined hollow morphology and uniform carbon coating, optimizing electrochemical activity. Electrochemical analysis reveals outstanding capacitance, enhanced performance even at elevated current densities, and long-term stability, making $NiCo_2O_4$@carbon hollow spheres a promising candidate for flexible, energy-dense supercapacitors. The material achieves a high specific capacitance of 733 F g^{-1} at 1 A g^{-1}, with minimal degradation over 5000 cycles, underscoring its potential in wearable electronics. This work highlights the effective use of MOF templates for creating hierarchical nanostructures, offering valuable insights into the rational design of flexible energy storage materials.

Introduction

Over recent years, there has been a significant shift toward the development of portable and flexible electronics, driven by the increasing demand for devices that are compact, lightweight, and capable of conforming to various shapes and applications.[1,2] Traditional batteries, while effective, often face limitations in terms of size, weight, and flexibility, thus motivating researchers to explore alternative energy storage solutions.[3] Among these alternatives, supercapacitors have emerged as a highly promising option. In particular, flexible asymmetric supercapacitors (ASCs) have attracted substantial attention due to their ability to combine electrode materials with complementary electrochemical properties, enabling enhanced energy storage while maintaining mechanical flexibility.[4,5]

Electrode materials for supercapacitors are primarily classified based on their charge storage mechanisms: double-layer capacitance and pseudo-capacitance. Materials that exhibit both types of mechanisms are considered ideal candidates for energy storage applications.[6–8] Nickel oxide (NiO) has long been regarded as a top-performing pseudocapacitive material owing to its high theoretical capacitance, large surface area, and versatile morphology. However, its electrochemical performance is hindered by issues such as poor cycling stability and low conductivity. To overcome these limitations, cobalt oxide (Co_3O_4) can be introduced to form a bimetallic nanocomposite. Cobalt oxide contributes excellent electroactive properties and improved cycling stability, making it an attractive component for advanced supercapacitor applications.[9,10]

One of the most promising bimetallic oxides in this context is nickel cobalt oxide ($NiCo_2O_4$, NCO), which has garnered significant interest due to its superior electrical conductivity,

[a]*Functional Nano-Materials (FuN) Laboratory, Department of Physics and Nanotechnology, Faculty of Engineering and Technology, SRM Institute of Science and Technology, Kattankulathur – 603203, India. E-mail: ajayrakkesh@gmail.com*
[b]*Department of Medical Physics, Anna University, Chennai – 600 025, India*
[c]*Department of Chemical Engineering, University of Seoul, Seoul 02504, Republic of Korea*
[d]*National Centre for Nanoscience and Nanotechnology, University of Madras, Chennai – 600 025, India*

†Electronic supplementary information (ESI) available: The Experimental section that includes materials, electrochemical testing and flexible ASC fabrication details alongside the equations used to perform several calculations. For pristine NCO@Cs, a schematic explanation of the preparation strategy and XPS spectra are provided. Three-electrode studies: voltammograms of NCO@C at higher scan rates; *b*-value, k_1 and k_2 obtained using the Dunns method; voltammograms distinguished by current contribution; specific capacitance over various current densities; *ex situ* analysis: XRD data and HRSEM images of cycled electrodes along with EDS results. Three-electrode studies on rGO. Two-electrode studies: CV curves, GCD data, and capacitance over various current densities and stability tests. Device fabrication and assembly and a Ragone plot with the respective data table. See DOI: https://doi.org/10.1039/d4nr04709e

enhanced redox properties, and cost-effectiveness. Despite its advantages over monometallic oxides, NCO faces challenges related to structural stability, which is crucial for long-term supercapacitor performance. Also, it is known that these bimetallic oxides are more susceptible to volumetric changes over cycling, which affects stability. In comparison, materials like sulfides and phosphides offer better stability, prompting the need for innovative strategies to improve NCO's performance.[11–14]

MOFs (metal–organic frameworks) have evolved as a dynamic solution for energy storage and environmental applications. Nickel–cobalt-based MOFs, in particular, offer unique architectures, large surface areas, tunable pore sizes, and excellent stability.[15] However, their poor electrical conductivity limits their direct application in energy storage. To address this issue, recent research has focused on deriving bimetallic oxides from partially carbonized MOFs.[16] Ren *et al*. synthesized ZnO@NiO and Co_3O_4@NiO composites from MOFs, leveraging the residual carbon from the organic framework. This residual carbon enhances electrical conductivity and mitigates volumetric changes, leading to superior pseudocapacitor performance. Similarly, Zhu *et al*. developed MOF-derived P–Co_3O_4@NC@Ov–NiMnLDH//CNT@ZIF-8-derived carbon, which exhibited remarkable specific capacitance and ultralong cycling stability, underscoring the material's enhanced durability. These studies demonstrate that partially carbonized metal oxides derived from MOFs effectively address critical challenges, such as poor electrical conductivity and volumetric changes. At the same time, enhanced pore connectivity improves overall stability.[17,18]

In this study, we report the synthesis of carbon-supported nickel cobalt oxide (NCO@C) derived from a bimetallic NiCo–BTC (benzene tricarboxylic acid) MOF. The synthesis involves a solvothermal method followed by partial carbonization under an inert atmosphere and subsequent oxidation in open air at high temperatures. This process yields carbon-supported NCO materials with high specific capacitance, superior conductivity and enhanced structural robustness. This approach provides a simple yet effective route to enhance the performance of NCO by leveraging the unique properties of MOF-derived carbon frameworks. Integrating NCO@C as an electrode material in flexible ASCs is expected to significantly improve energy storage performance. This potential is explored through comprehensive structural and electrochemical characterization, demonstrating the material's feasibility for real-world flexible energy storage applications.

Materials and methods

Synthesis of NiCo–BTC microspheres

The synthesis process begins by dissolving $Ni(NO_3)_2{\cdot}6H_2O$ and $Co(NO_3)_2{\cdot}6H_2O$ in a 1 : 2 molar ratio in 40 ml of DMF. Concurrently, 0.315 g of trimesic acid is added to the solution containing the dissolved metal salts, and the mixture is stirred for 30 minutes to ensure complete dissolution. The resulting solution is then transferred to a 100 ml Teflon-lined stainless-steel autoclave and heated at 150 °C for 12 hours. After the reaction, the autoclave is allowed to cool naturally. The obtained product is rinsed with ethanol and centrifuged four times to remove any residual impurities. The sample is then dried overnight at 80 °C in a hot air oven. Finally, the dried powder is collected, thoroughly ground using a mortar and pestle, and prepared for various characterization studies.

Synthesis of $NiCo_2O_4$ derived from NiCo–BTC

NiCo–BTC (0.5 g) was placed in an alumina boat and positioned inside a tubular furnace. The sample underwent annealing at 350 °C for 30 minutes under an argon atmosphere. Following this, the sample was further annealed at 400 °C for 2 hours under open-air conditions to ensure complete oxidation (as shown in Fig. S1†). After the annealing process, the samples were collected, finely ground using a mortar and pestle, and prepared for subsequent characterization.

Characterization

The obtained samples were thoroughly characterized using various analytical techniques. X-ray diffraction (XRD) was performed with a PANalytical powder diffractometer using Cu Kα radiation to confirm the crystal structure. Fourier transform infrared spectroscopy (FTIR) was conducted with a Shimadzu IR Tracer 100 spectrometer, covering an infrared (IR) range from 400 to 4000 cm^{-1}, to identify functional groups. The surface chemistry of the samples was analyzed using X-ray photoelectron spectroscopy (XPS) with a PHI-VERSAPROBE III instrument. For morphological and compositional analysis, high-resolution scanning electron microscopy (HRSEM) was employed using a Thermo Scientific Apreo S instrument, while high-resolution transmission electron microscopy (HRTEM) was performed using a JEOL JEM-2100 Plus. The specific surface area of the samples was determined through nitrogen (N_2) adsorption–desorption measurements using the Brunauer–Emmett–Teller (BET) method with a Micromeritics ASAP 2020 surface area analyzer. The electrochemical behavior of the $NiCo_2O_4$ microspheres was examined using cyclic voltammetry (CV), galvanostatic charge–discharge (GCD), and electrochemical impedance spectroscopy (EIS). These measurements were carried out on an OrigaFlex OGF05A electrochemical workstation, utilizing a three-electrode system, with platinum wire as the counter electrode and Ag/AgCl as the reference electrode.

Preparation of electrodes for three and two electrode studies

The preparation of the working electrode involved loading a vial with a mixture of 90 wt% of the active material, 5 wt% polyvinylidene fluoride (PVDF) as the binder, and 5 wt% carbon black as the conductive additive. This mixture was thoroughly blended with *N*-methyl-2-pyrrolidone (NMP) solvent until it formed a slurry. The resulting slurry was then uniformly applied onto a 0.5 × 0.5 cm area of nickel foam (NF) using a brushing technique. Prior to coating, the nickel foam

was weighed and labeled as 'E_w'. After the coating was dried, the electrodes were weighed again, labeled as 'E_{cw}', and the weight of the active material was calculated by subtracting 'E_w' from 'E_{cw}'.

Results and discussion

The structural characterization of NCO@C derived from NiCo–BTC was conducted using X-ray diffraction (XRD) (Fig. 1a). The XRD patterns confirm the successful formation of bimetallic oxides, with high-intensity peaks corresponding to NiCo–BTC no longer visible. Instead, new peaks were observed at 2θ values of 19.11°, 31.30°, 36.84°, 44.86°, 59.39°, and 65.23°, and indexed with corresponding Miller indices from (111) to (440) owing to the cubic spinel structure of $NiCo_2O_4$, which coincides with JCPDS #20-0781. These diffraction planes further corroborate the formation of the desired bimetallic oxide phase. Notably, the absence of carbon peaks in the diffractogram indicates that the carbon present is in an amorphous form.

Further confirmation was obtained *via* Fourier-transform infrared (FTIR) spectroscopy, as revealed in Fig. 1b. The spectrum of NiCo–BTC displays peaks at 1355 and 1605 cm^{-1}, corresponding to the symmetric (ν_s) and asymmetric (ν_{as}) stretching of carboxyl groups from trimesic acid, confirming the effective coordination of –COO groups with the metal center in a bidentate fashion.[19,20] Additionally, peaks at 1058, 757, and 1556 cm^{-1} were owing to the aromatic ring's stretching vibrations. At lower wavenumbers, bands at 466 and 534 cm^{-1} correspond to Ni–O and Co–O bond stretching vibrations, providing further evidence of the successful formation of NiCo–BTC. The FTIR analysis of the NCO@C sample reveals broad bands at 641 and 560 cm^{-1}, attributed to metal–oxygen (M–O) vibrations, while bands at 1599 and 1394 cm^{-1} are associated with C–C and C–O vibrations.[21,22]

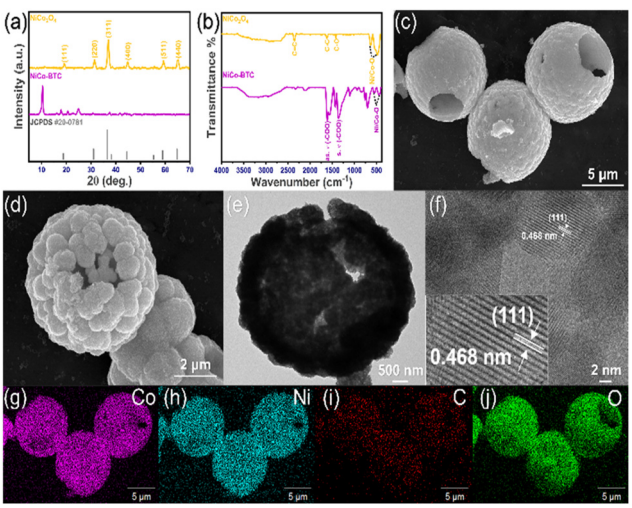

Fig. 1 (a) X-ray diffractograms of NiCo–BTC and $NiCo_2O_4$ along with the JCPDS card. (b) Infrared spectra of NiCo–BTC and $NiCo_2O_4$. (c & d) Micrographs of the NCO@C microspheres at various resolutions. (e & f) TEM images showcasing similar morphologies and respective lattice planes. (g–j) Elemental mapping of various atoms present in NCO@C.

The morphology and structure of NCO@C were examined using scanning electron microscopy (SEM) (Fig. 1c and d), which revealed that the NCO particles have a uniform size distribution and shape. The MOF template played a crucial role in forming the hollow spherical structures, which are composed of smaller spherical crystallites. These crystallites, oriented in various directions, aggregate to form hollow spheres with rough outer surfaces. The SEM images at different resolutions are provided in Fig. 1c and d. At lower resolution, the SEM images reflect the spherical structure with a rough exterior. The aggregated spheres can be distinctly seen at higher resolution, revealing their outer rough surfaces. The elemental mapping (Fig. 1g–j) further confirms the presence and distribution of Ni, Co, and O within the structure.

Transmission electron microscopy (TEM) analysis corroborates the formation of the hollow spherical structures, showcasing a high degree of crystallinity at the atomic level. Fig. 1e and Fig. S3† display the successful formation of the spherical morphology through the assembly of the crystallite particles. The clear interior and denser exterior of NCO@C exhibit the hollow structure formed due to the agglomerated crystallite particles with overall spherical morphology. At higher resolution, the crystallite particles with different orientations agglomerated to form the spherical hollow structure, as can be seen in Fig. 1f. The lattice fringes observed in the TEM images correspond to the (111) planes, with an interplanar spacing of 0.23 nm, further validating the formation of $NiCo_2O_4$ in line with the XRD results. The hollow structure, well-defined morphology, and uniform size further emphasize the successful transformation of NiCo–BTC into NCO@C.

The XPS analysis of the carbonized hollow NCO@C spheres confirmed the presence of Co, Ni, O, and C elements fitted with the Gaussian–Lorentzian function and provided valuable insights into their oxidation states. The deconvoluted Co 2p spectrum displayed two spin–orbit components, Co $2p_{3/2}$ and Co $2p_{1/2}$, with binding energies at 779.4 eV and 794.6 eV, respectively, corresponding to the Co^{3+} oxidation state. Additionally, the peaks detected at 781.4 eV and 797.1 eV were ascribed to the Co^{2+} oxidation state. Similarly, the Ni 2p spectrum exhibited spin–orbit components at 853.7 eV and 855.6 eV for Ni $2p_{3/2}$ and at 870.9 eV and 873.1 eV for Ni $2p_{1/2}$, characteristic of the Ni^{3+} and Ni^{2+} oxidation states. The dual presence of Co^{3+}/Co^{2+} and Ni^{3+}/Ni^{2+} redox pairs plays a pivotal role in enhancing the charge storage capabilities of the material. The higher oxidation states (Co^{3+} and Ni^{3+}) are particularly advantageous, as they promote increased charge mobility and improve redox kinetics at the electrode–electrolyte interface, resulting in superior electrochemical performance. Furthermore, the facile transition between these oxidation states enables rapid faradaic reactions, essential for achieving high specific capacitance in charge storage applications. These observations align with previous studies that emphasize the significance of mixed-valence states in augmenting the pseudocapacitive behavior of metal oxides.[23–26]

The oxygen 1s spectrum (Fig. S2b†) revealed three distinct peaks: O_1 at 529.4 eV, corresponding to metal–oxygen bonds (M–O), O_2 at 530.9 eV, attributed to oxygen ions (O^{2-}), and O_3 at 532.4 eV, representing chemisorbed oxygen and under-coordinated lattice oxygen, which play a key role in improving surface reactivity. The carbon 1s spectrum displayed peaks at binding energies of 284.8 eV, 285.2 eV, and 288.5 eV, and the peaks were associated with C–C, C–O, and lastly with C═O, respectively, confirming the successful partial carbonization of the material, which enhances the conductivity of the composite (Fig. 2a–c).[27,28]

Further insights into the surface area and porosity of the NCO@C microspheres were obtained using N_2 adsorption/desorption isotherms. The curves exhibited a type IV isotherm with a well-defined hysteresis loop at high pressures, indicative of a mesoporous structure. The NCO@C spheres demonstrated a large BET surface area of 91 $m^2\ g^{-1}$, significantly higher than typical bimetallic oxides. The pore size distribution study (BJH) revealed pore sizes primarily in the range of 2–10 nm, further confirming the mesoporous architecture. This high pore volume and mesoporosity facilitate the rapid diffusion of OH^- ions (from the electrolyte) into the microspheres, enhancing the performance of the material. The optimized mesoporous structure allows for effective faradaic reactions, promoting efficient ion exchange and charge storage within the electrode material (Fig. 2d).[29]

The electrochemical behaviour of the NCO microspheres coated on nickel foam (NiF) was systematically investigated using a three-electrode setup. Cyclic voltammetry (CV) was performed at various scan rates (ν), ranging from 2 to 50 mV s^{-1}. Voltammograms for the scan rates from 10 to 50 mV s^{-1} are shown in Fig. S4,† with a potential window of 0.7 V (Fig. 3a). Distinct redox peaks corresponding to reduction and oxidation processes are evident, indicating the occurrence of redox reactions between Ni/Co–O and hydroxyl ions. As the scan rate increases beyond 20 mV s^{-1}, the electrode displays a mix of faradaic pseudocapacitance and double-layer capacitance, with the latter becoming more dominant at higher rates, likely due to partial carbonization. At lower scan rates, the faradaic pseudocapacitance is more pronounced. To explore the redox behavior of the NCO microspheres in greater detail, scan rates ranging from 2 to 10 mV s^{-1} were employed.

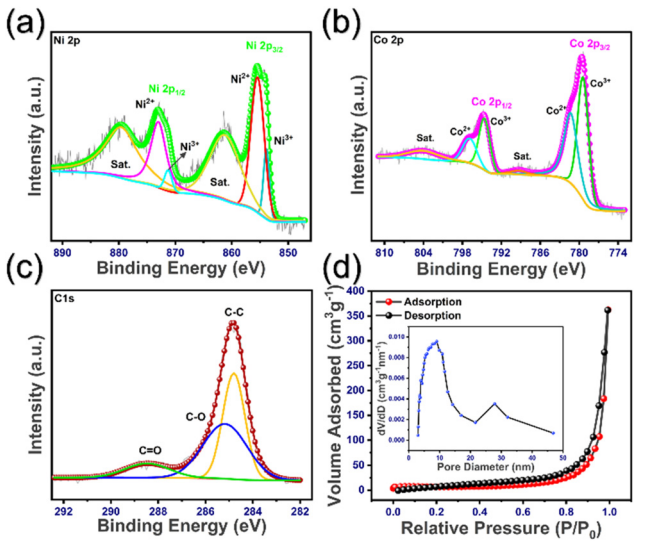

Fig. 2 (a) XPS spectra revealing the surface chemistry of nickel 2p, (b) cobalt 2p & (c) carbon 1s. (d) N_2 adsorption–desorption analysis of NCO@C (inset: pore size distribution profile).

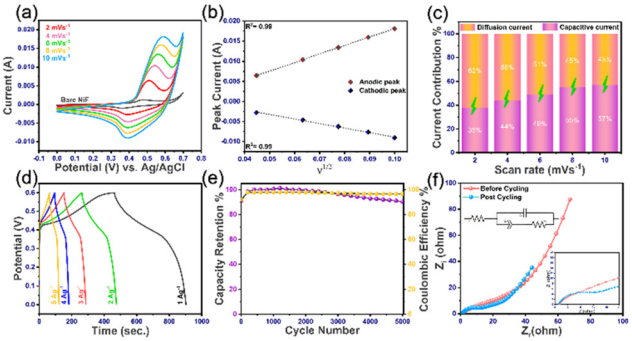

Fig. 3 (a) Voltammograms at various scan rates. (b) Correlation between the peak current and the square root of the scan rate. (c) Current contribution at distinct scan rates using Dunn's method. (d) Charge–discharge curves. (e) Cycling stability over 5000 cycles. (f) Impedance spectra revealing the intrinsic properties of the NCO@C electrodes.

The correlation between the peak current (i_p) and the square root of the scan rate ($\nu^{1/2}$) for both anodic and cathodic responses was analyzed using the Randles–Sevcik equation (Fig. 3b).[30] As the scan rate increases, the anodic peaks shift to higher positive potentials, and the cathodic peaks move to lower negative potentials. This shift signifies strong electrochemical reversibility and improved potential separation, indicating enhanced redox activity. Specifically, at scan rates between 2 and 10 mV s^{-1}, the anodic peak shifts from 0.51 V to 0.59 V, a minor variation of 0.08 V, suggesting that the NCO@C microspheres exhibit excellent electrode reaction kinetics. This behaviour is attributed to the highly conductive nature of the carbon matrix and the increased surface area due to partial carbonization.

The *b*-value, obtained from the equation $i_p = a\nu^b$, provides insight into the charge storage mechanism. The slope of the $\log(i_p)$ *versus* $\log(\nu)$ plot was found to be 0.641 (Fig. S5a†), suggesting a mixed charge storage mechanism that is intermediate between diffusion-controlled and capacitive behaviour. A *b*-value closer to 0.5 indicates that the charge storage mechanism is primarily pseudocapacitive. To further quantify the contributions of surface-controlled and diffusion-governed processes, Dunn's method was applied. As shown in the bar graph (Fig. 3c), the current resulting from diffusion-controlled faradaic reactions is dominant at 2 mV s^{-1}, while capacitive contributions increase with scan rate, rising from 38% at 2 mV s^{-1} to 57% at 10 mV s^{-1}. This trend can be attributed to the increasing diffusion resistance and the presence of carbon. The CV plots at 2 mV s^{-1} and 10 mV s^{-1}, illustrating the

current contributions, are presented in Fig. S6.†[31,32] These findings underscore the significant role of partial carbonization in enhancing the capacitive behaviour of NCO@C microspheres while also enabling excellent pseudocapacitive performance at lower scan rates.

The charge–discharge (GCD) curves, as shown in Fig. 3d, were measured across a range of current densities, confirming the pseudocapacitive nature of the NCO@C electrode. The specific capacitance values, calculated at current densities ranging from 1 to 5 A g^{-1} (as shown in Fig. S7†), were determined to be 733, 701, 659, 578, and 486 F g^{-1}, respectively. These values underscore the remarkable electrochemical performance of NCO@C, due to the synergistic interaction of Ni and Co atoms, exhibiting multiple valence states and facilitating faradaic reactions. Additionally, the carbon matrix plays a crucial role in enhancing conductivity, thereby improving charge transport and storage capabilities. The electrochemical reaction responsible for the charge storage behaviour of NCO can be described by the following redox reactions:[33,34]

$$NiCo_2O_4 + OH^- + H_2O \leftrightarrow NiOOH + 2CoOOH + e^-$$

$$CoOOH + OH^- \leftrightarrow CoO_2 + H_2O + e^-$$

$$NiCo_2O_4 + 3OH^- \leftrightarrow NiOOH + 2CoO_2 + H_2O + 3e^-$$

The stability and coulombic efficiency (CE) of the NCO@C electrode material were evaluated by subjecting it to 5000 charge–discharge cycles. After cycling at a current density of 10 A g^{-1}, the electrode exhibited a capacity retention of 90.3% and a CE of 95.5%, reflecting its enhanced stability compared to similar reported studies (Fig. 3e). Notably, the specific capacitance of NCO@C demonstrated a slight improvement over previously reported works, further underscoring its superior electrochemical performance. To explore in greater detail the electron-transfer dynamics, interfacial interactions, and capacitive characteristics of the electrode material, impedance spectroscopy was performed across a frequency range of 100 kHz to 10 mHz, with the resulting Nyquist plot presented in Fig. 3f. Analysis of the Nyquist plot using the equivalent circuit (inset of Fig. 3f) provided valuable insights into the material's resistive and capacitive behaviour. The intrinsic resistance (R_s) of the active material on NiF is measured by finding the intercept on the real axis in the high-frequency region, which was measured at 1.36 Ω before cycling and slightly reduced to 1.2 Ω after cycling. This reduction indicates the material's robustness and low internal resistance.[35]

The semicircular region of the plot corresponds to the charge transfer resistance (R_{ct}) at the electrode–electrolyte interface, which exhibited a minor increase post-cycling, suggesting stable charge transfer properties. At lower frequencies, the Warburg resistance 'R_w' represents the ion diffusion resistance within the electrode's architecture. The steep slope at low frequencies indicates capacitive behaviour akin to that of an ideal capacitor, with minimal diffusion resistance. After cycling, this slope became slightly steeper, pointing to efficient electrolyte ion diffusion through the porous structure of the NCO@C microspheres, which minimizes ion diffusion resistance and enhances the electrode's capacitive performance. These results demonstrate that the NCO@C electrode possesses rapid charge transfer kinetics, reduced intrinsic resistance, and excellent conductivity, aligning with findings from previous studies.[34,36] Post-cycling structural studies, including *ex situ* diffraction analysis and electron microscopy, were carried out to further assess the material's stability. Fig. S8(a and b)† presents the X-ray diffraction patterns, where the observed peaks correspond to $NiCo_2O_4$ and the Ni foam substrate on which the active material is coated. The diffraction peaks at 31.13° and 36.72°, assigned to the (220) and (311) planes of $NiCo_2O_4$, confirm the structural stability of the material with no phase changes even after 5000 charge–discharge cycles. Furthermore, the scanning electron microscopy (SEM) images (Fig. S9†) demonstrate minimal damage to the spherical morphology of the material post-cycling. Energy-dispersive spectroscopy (EDS) analysis shows the presence of Ni, Co, O, C, and traces of K, the latter attributable to K^+ ions from the electrolyte. These findings collectively establish the exceptional structural and morphological stability of the $NiCo_2O_4$@C electrode, making it a highly durable and reliable material for supercapacitor applications.

To demonstrate the practical application of the prepared materials, a flexible asymmetric supercapacitor (ASC) was constructed using NCO@C as the cathode and rGO as the anode, both coated on a flexible nickel substrate, with PVA/KOH gel serving as the electrolyte. Before assembling the flexible ASC, the electrochemical performance of rGO as the anode and NCO@C as the cathode was evaluated in a two-electrode setup using aqueous KOH as the electrolyte. This configuration delivered a remarkable specific capacitance of 213 F g^{-1} at a current density of 1 A g^{-1}, along with excellent cycling stability, retaining 89% of its initial capacitance after 5000 cycles at 6 A g^{-1} (Fig. S12†). These outcomes underscore the synergistic interaction of the NCO@C and rGO combination, which prompted the construction of the flexible device (Fig. S13†). The flexible ASC was subsequently tested across various scan rates and current densities, with the corresponding cyclic voltammetry (CV) and galvanostatic charge–discharge (GCD) profiles showing well-defined peaks (represented in Fig. 4a–d). As the scan rate progressed, the broadening of these peaks indicated contributions from both the pseudocapacitive behaviour of NCO@C and the surface capacitive nature of rGO. The GCD analysis revealed that the device achieved a peak specific capacitance of 46 F g^{-1} at 1 A g^{-1}. Furthermore, the device displayed a peak power density of 2.25 kW kg^{-1} and an energy density of 14.36 W h kg^{-1}, highlighting its potential for high-performance energy storage.

Long-term cycling tests demonstrated the robustness of the ASC, with ~84% capacitance retention going past 5000 cycles and a CE of 98%. The stability and efficiency of the device suggest its suitability for powering portable electronic devices. To further showcase its real-world applicability, the ASC was successfully used to power red LEDs and an alarm clock (Fig. 4e and f), emphasizing the promise of these electrode materials for flexible energy storage applications.

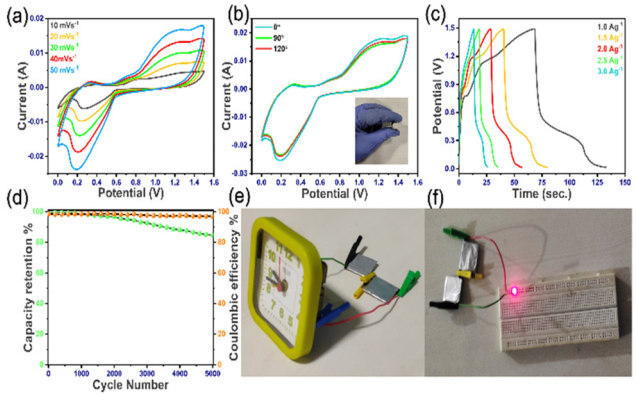

Fig. 4 (a & b) Voltammograms for various scan rates and bending angles. (c) Charge–discharge curves over various current densities. (d) Capacity retention over 5000 cycles@5A g^{-1}. (e & f) Analog clock and LEDs powered using the fabricated ASC.

Conclusions

In summary, this study successfully demonstrates the formation of $NiCo_2O_4$@C microspheres derived from NiCo–BTC *via* partial carbonization, with detailed structural analysis confirming their hollow, micro-spherical morphology, alongside highly mesoporous architecture and vast surface area. The electrochemical evaluation of $NiCo_2O_4$@C revealed a remarkable specific capacitance of 733 F g^{-1} at 1 A g^{-1} and excellent cycling stability, retaining 90.3% of its capacitance over 5000 cycles. *Ex situ* XRD and SEM analyses confirmed the structural integrity of the material after cycling, further emphasizing its robustness. In two-electrode configurations with reduced graphene oxide (rGO) as the anode, the combination of these materials significantly enhanced overall device performance, demonstrating their synergistic effect in energy storage. The design and testing of a flexible asymmetric supercapacitor (ASC) using $NiCo_2O_4$@C microspheres and rGO showcased their practical applicability, underscoring the possibilities offered by these materials for high-performance, flexible energy storage devices. These findings highlight the critical role of $NiCo_2O_4$@C microspheres in advancing supercapacitor technology for real-world applications.

Author contributions

T. B. N.: conceptualization and writing – original draft. D. D.: investigation and validation. M. R. A. K.: investigation and validation. B. S.: validation. A. R. R.: formal analysis, validation, investigation, supervision and conceptualization.

Data availability

The data supporting this article have been included as part of the ESI.†

Conflicts of interest

The authors declare no conflicts of interest.

Acknowledgements

The authors gratefully acknowledge the funding support provided by the Anusandhan National Research Foundation, Department of Science and Technology (DST), under sanction no.: EEQ/2023/000314. Author A. R. R. extends appreciation to UGC-BSR for the start-up research grant (UGC ref. no: F. 30-524/2020 (BSR)), which provided additional support. Author T. B. N. expresses gratitude to SRMIST for the financial assistance through the SRM fellowship. The authors also wish to acknowledge the invaluable assistance of the SRM Central Instrumentation Facility (SCIF), the Nanotechnology Research Center (NRC), and the Physics and Nanotechnology Characterization Facility (PNCF) for providing access to their advanced characterization equipment.

References

1 Y. Wang, X. Wu, Y. Han and T. Li, *J. Energy Storage*, 2021, **42**, 103053.
2 S. Cho, J. Lim and Y. Seo, *ACS Omega*, 2022, **7**, 37285–37833.
3 P.-C. Chen, G. Shen, Y. Shi, H. Chen and C. Zhou, *ACS Nano*, 2010, **4**, 4403–4411.
4 T. B. Naveen, D. Durgalakshmi, A. K. Kunhiraman, S. Balakumar and R. Ajay Rakkesh, *J. Mater. Res.*, 2021, **36**, 4102–4119.
5 T. Liu, C. Jiang, B. Cheng, W. You and J. Yu, *J. Power Sources*, 2017, **359**, 371–378.
6 M. Liu, J. Chang, J. Sun and L. Gao, *RSC Adv.*, 2013, **3**, 8003.
7 S. Zheng, X. Li, B. Yan, Q. Hu, Y. Xu, X. Xiao, H. Xue and H. Pang, *Adv. Energy Mater.*, 2017, **7**, 1602733.
8 G. Zhu, H. Wen, M. Ma, W. Wang, L. Yang, L. Wang, X. Shi, X. Cheng, X. Sun and Y. Yao, *Chem. Commun.*, 2018, **54**, 10499–10502.
9 L. Kumar, M. Chauhan, P. K. Boruah, M. R. Das, S. A. Hashmi and S. Deka, *ACS Appl. Energy Mater.*, 2020, **3**, 6793–6804.
10 Y. Li, X. Han, T. Yi, Y. He and X. Li, *J. Energy Chem.*, 2019, **31**, 54–78.
11 H. Wang, P. Zhao, X. Zhang, X. Lu, Z. Qiu, K. Ren, Z. Xu, R. Yao, T. Wei and Z. Fan, *Nano Res.*, 2022, **15**, 9047–9056.
12 P. N. Blessy Rebecca, D. Durgalakshmi, S. Balakumar and R. Ajay Rakkesh, *Chem. Eng. J.*, 2024, **484**, 149789.
13 R. Saha, K. Gupta and C. J. Gomez Garcia, *Cryst. Growth Des.*, 2024, **24**, 2235–2265.
14 N. Alhokbany, J. Ahmed, M. Ubaidullah, S. Mutehri, M. A. M. Khan, T. Ahamad and S. M. Alshehri, *J. Mater. Sci.: Mater. Electron.*, 2020, **31**, 16701–16707.

15 X. Yang, X. Zhang, N. Yang, L. Yang, W. Wang, X. Fang and Q. He, *Molecules*, 2023, **28**, 5613.
16 X.-. Y. Yu, X.-Z. Yao, T. Luo, Y. Jia, J.-H. Liu and X.-J. Huang, *ACS Appl. Mater. Interfaces*, 2014, **6**, 3689–3695.
17 Y.-F. Ren, Z.-L. He, H.-Z. Zhao and T. Zhu, *Rare Met.*, 2022, **41**, 830–835.
18 F. Zhu, L. Sun, Y. Liu and W. Shi, *J. Mater. Chem. A*, 2022, **10**, 21021–21030.
19 X. Wang, Q. Li, N. Yang, Y. Yang, F. He, J. Chu, M. Gong, B. Wu, R. Zhan and S. Xiong, *J. Solid State Chem.*, 2019, **270**, 370–378.
20 Q. Li, X. Wang, N. Yang, F. He, Y. Yang, B. Wu, J. Chu, A. Zhou and S. Xiong, *Anorg. Allg. Chem.*, 2019, **645**, 1022–1030.
21 L. Kumar, H. Chauhan, N. Yadav, S. A. Hashmi and S. Deka, *ACS Appl. Energy Mater.*, 2018, **1**, 6999–7006.
22 A. M. Al-Enizi, M. Ubaidullah, J. Ahmed, T. Ahamad, T. Ahmad, S. F. Shaikh and M. Naushad, *Composites, Part B*, 2020, **183**, 107655.
23 T. Liu, S. Zhou, X. Yu, C. Mao, Y. Wei, X. Yu, L. Chen, X. Zhao, G. Tian and L. Chen, *RSC Adv.*, 2022, **12**, 4029–4041.
24 G. Guo, Y. Mei, X. Chen, J. Liu and W. Liu, *RSC Adv.*, 2023, **13**, 25018–25028.
25 Y. Wang, L. Chen, H. Zhang, M. Humayun, J. Duan, X. Xu, Y. Fu, M. Bououdina and C. Wang, *Green Chem.*, 2023, **25**, 8181–8195.
26 Y. Ha, L. Shi, X. Yan, Z. Chen, Y. Li, W. Xu and R. Wu, *ACS Appl. Mater. Interfaces*, 2019, **11**, 45546–45553.
27 D. Yang, Q. Zhao, L. Huang, B. Xu, N. A. Kumar and X. S. Zhao, *J. Mater. Chem. A*, 2018, **6**, 14146–14154.
28 V. Raman, N. V. Mohan, B. Balakrishnan, R. Rajmohan, V. Rajangam, A. Selvaraj and H.-J. Kim, *Ionics*, 2020, **26**, 345–354.
29 Y. Liu, Z. Wang, Y. Zhong, M. Tade, W. Zhou and Z. Shao, *Adv. Funct. Mater.*, 2017, **27**, 1701229.
30 T. Selvam, D. Dhinasekaran, B. Subramanian and A. R. Rajendran, *Appl. Phys. Lett.*, 2024, **124**, 073906.
31 T. B. Naveen, D. Durgalakshmi, S. Balakumar and R. Ajay Rakkesh, *Chem. Commun.*, 2024, **60**, 208–211.
32 S. Raj, S. K. Srivastava, P. Kar and P. Roy, *RSC Adv.*, 2016, **6**, 95760–95767.
33 X. Y. Liu, Y. Q. Zhang, X. H. Xia, S. J. Shi, Y. Lu, X. L. Wang, C. D. Gu and J. P. Tu, *J. Power Sources*, 2013, **239**, 157–163.
34 S. Gao, F. Liao, S. Ma, L. Zhu and M. Shao, *J. Mater. Chem. A*, 2015, **3**, 16520–16527.
35 T. Selvam, D. Dhinasekaran, B. Subramanian and A. R. Rajendran, *J. Phys. Chem. Lett.*, 2024, **15**, 1338–1346.
36 Y. Wang, D. Liu and K. Cao, *J. Porous Mater.*, 2018, **25**, 565–570.